Chapter 15

Video-Based Kinetic Analysis of Period Variations and Oscillation Patterns in the Ce/Fe-Catalyzed Four-Color Belousov–Zhabotinsky Oscillating Reaction

Rainer Glaser,[1,2,*] Marco Downing,[2,3] Ethan Zars,[1] Joseph Schell,[1,2] and Carmen Chicone[3]

[1]Department of Chemistry, Missouri University of Science and Technology, Rolla, Missouri 65409, United States

[2]Department of Chemistry, University of Missouri, Columbia, Missouri 65211, United States

[3]Department of Mathematics, University of Missouri, Columbia, Missouri 65211, United States

[*]E-mail: glaserr@mst.edu; glaserr@missouri.edu

The development of a video-based method for the measurement of the kinetics of oscillating reactions is described in this chapter. The method mimics reflection ultraviolet–visible spectroscopy and allows for simultaneous measurement at any target color (R_C, G_C, B_C) with a temporal resolution of 0.01 s. The image analysis results in discrete time traces [$DCC(t, R_C, G_C, B_C)$], and numerical methods are described for the analysis of the quasiperiodic oscillation patterns over the course of the reactions to determine period lengths $PT(t)$ and other parameters [oxidation times $OT(t)$, reduction times $RT(t)$, etc.] that characterize the redox chemistry of the catalysts within each period. The methods were demonstrated with studies of the Ce/Fe-catalyzed four-color Belousov–Zhabotinsky reactions. The temporal evolution of period and pattern characteristics are described with polynomials, and values measured for reaction times of approximately 500 and 2000 s are discussed to highlight the temporal changes. The measurements provide a wealth of constraints to determine chemically reasonable reaction models. The discovery of the Bactrian-type oscillation pattern of ferriin in the four-color Belousov–Zhabotinsky reactions is a key result of the present study: the concentration of Fe^{3+} goes through two maxima in every period.

Introduction

The original Belousov–Zhabotinsky (BZ) oscillating reaction referred to the cerium-catalyzed bromate oxidation of citric acid (*1*–*9*). Today, the term describes the entire class of bromate

Towns et al.; It's Just Math: Research on Students' Understanding of Chemistry and Mathematics
ACS Symposium Series; American Chemical Society: Washington, DC, 2019.

oxidations of dicarboxylic acids (malonic acid, malic acid, etc.) catalyzed by a variety of metals including Fe (*10*). BZ oscillating reactions are the prototypical nonlinear chemical systems (*11*–*16*). To fully understand these reactions requires the ability to simulate their kinetics without any simplifying assumptions while considering consumption of substrates and the formation of a myriad of products—a daunting challenge. To approach such complexity requires experimental studies of the reaction kinetics, mechanistic studies to explore plausible reaction mechanisms, and computational simulations of the complete multiequilibria systems. Occasional collaboration of chemists with mathematicians will not suffice; the approach requires faculty and students with a thorough understanding of both chemistry and mathematics.

A few years ago, a group of faculty (including the corresponding author) won a National Science Foundation Proactive Recruitment in Introductory Science and Mathematics (PRISM) grant in mathematics and life sciences to promote the integration of mathematics education with science education. The program involved various components, including freshman interest groups, new research-oriented courses and interdisciplinary seminars, and, importantly, early undergraduate research experiences. In this context, two of the authors (Rainer Glaser and Carmen Chicone) created a nonlinear dynamics group to study the mechanism of BZ oscillating reactions using a combination of experimental, computational, and mathematical methods. The group studied aspects of bromine chemistry (*17*, *18*), and attention quickly turned to questions about pH dependence (*17*, *19*, *20*). In parallel, the group learned how to solve multiequilibria problems (*21*), learned how to include effects of ionic strength (*22*, *23*), and explored spectral decomposition (*24*). In 2018, these pieces came together in a study of the Fe-catalyzed BZ reaction, which, for the first time, achieved agreement between experiments and simulations of the pH dependence over a wide range (*25*).

In this chapter, we present the results of a video-based kinetic analysis of the four-color BZ oscillating reaction (FC-BZR) and an analysis of the temporal evolution of the oscillation pattern. The new method for video analysis of chemical reactions mimics reflection ultraviolet–visible (UV-vis) spectroscopy and allows for the study of fast reactions at any wavelength at the same time. This video-based kinetic analysis was applied to the Ce/Fe-catalyzed FC-BZR. An oscillation pattern analysis is described for the characterization of dromedary- and Bactrian-type time traces, and the effects of color-base selection are analyzed in detail. The result of the analyses is a wealth of discrete experimental data for period lengths, oxidation times, and reduction times for every reaction as a function of reaction time, as well as regression functions that describe the temporal evolution of the characteristic parameters. A chemical reaction mechanism is discussed to explain the Bactrian-type oscillation pattern of the Fe catalysts. A full and quantitative understanding of the details of FC-BZR will require simulations of the entire reaction system, and the measured data provide a wealth of experimental constraints to determine chemically reasonable parameters.

Ce/Fe-Catalyzed FC-BZR

The Ce/Fe-catalyzed BZ oscillating reaction has attracted much interest, and the chemistry greatly depends on the Ce/Fe concentration ratio (*26*–*30*). Lefelhocz (*26*) described the original Ce/Fe-catalyzed BZ reaction by adding an iron catalyst to Bruice and Kasperek's Ce-BZR (*27*); this system with [Ce]/[Fe] ≈ 1 results in oscillations between purple and blue. Citing unpublished work by Rossman, Lefelhocz mentions that a higher Ce/Fe concentration ratio of approximately 10 results in red–green oscillations, the so-called traffic light reaction. In this spirit, the purple–blue system was described as the "alternative traffic light." Ruoff et al. (*28*) explored similar systems with even higher Ce/Fe concentration ratios and observed red–blue or red–green oscillations, and D'Alba and

Di Lorenzo (*29*, *30*) explored various purple–blue systems with low Ce/Fe concentration ratios. The FC-BZR shows a spectacular oscillation in that the solution periodically cycles through four colors in the sequence red, blue, green, blue, and purple. The reaction has been described by Shakhashiri (*31*) and has become a popular demonstration reaction.

The colors in Shakhashiri's FC-BZR are caused by the different oxidation states of the iron and cerium ions (Table 1). The solution starts out red because both metals are present in their reduced states, and it turns blue for the first time because Fe(II) is oxidized quickly to Fe(III). Soon thereafter, the cerium is oxidized and the solution turns green because both iron and cerium are present mostly in their oxidized states. Cerium does not stay oxidized for long, and the solution goes back to blue because the iron remains mostly oxidized while Ce(IV) is undergoing reduction to Ce(III). The solution gradually moves toward red as the number of Fe(II) ions increases. This changing proportion of Fe(III) ions to Fe(II) ions is visible as a purple solution gradually becoming red. After all the iron is reduced, the cycle begins anew.

Table 1. Observed Colors of the FC-BZR, Characteristic Values (R_C, G_C, B_C), and Dominant Metal Ions at the Various Color Phases

Color	*Iron*	*Cerium*	R_C	G_C	B_C
Red	Fe(II)	Ce(III)	0.764706	0.035294	0.039216
Blue1	Fe(III)	Ce(III)	0.072606	0.187665	0.390992
Green	Fe(III)	Ce(IV)	0.261962	0.858040	0.140393
Blue2	Fe(III)	Ce(III)	0.139660	0.338500	0.657990
Purple	Fe(II)/(III)	Ce(III)	0.639216	0.282353	1.000000
Yellow	N/A	Ce(IV)	0.962219	0.928007	0.105122

$$2\ BrO_3^- + 12\ H^+ + 10\ Fe^{2+} \rightleftarrows Br_2 + 6\ H_2O + 10\ Fe^{3+} \quad (1)$$

$$2\ BrO_3^- + 12\ H^+ + 10\ Ce^{3+} \rightleftarrows Br_2 + 6\ H_2O + 10\ Ce^{4+} \quad (2)$$

$$BrCH(COOH)_2 + 2\ H_2O + 4\ Fe^{3+} \rightleftarrows HCOOH + 2\ CO_2 + Br^- + 4\ Fe^{2+} + 5\ H^+ \quad (3)$$

$$BrCH(COOH)_2 + 2\ H_2O + 4\ Ce^{4+} \rightleftarrows HCOOH + 2\ CO_2 + Br^- + 4\ Ce^{3+} + 5\ H^+ \quad (4a)$$

$$H_2C(COOH)_2 + 2\ H_2O + 6\ Ce^{4+} \rightleftarrows HCOOH + 2\ CO_2 + 6\ Ce^{3+} + 6\ H^+ \quad (4b)$$

$$Ce^{4+} + Fe^{2+} \rightleftarrows Ce^{3+} + Fe^{3+} \quad (5)$$

The sequence of the color changes can be explained by eqs 1–5. Equations 1 and 2 describe the oxidations of Fe^{2+} and Ce^{3+} by bromate, respectively. Bromine generated in eqs 1 and 2 will brominate malonic acid (MA) to bromomalonic acid [BMA, $BrCH(COOH)_2$]. The systems studied here all start with large amounts of BMA present because the combination of bromate and bromide leads to an initial Br_2 burst and the conversion of MA to BMA. Equations 3 and 4a describe the

reductions of Fe^{3+} and Ce^{4+} by BMA, respectively. While ferriin does not oxidize MA, Ce^{4+} can (eq 4b). The reduction standard potentials for the redox couples Fe(III)/Fe(II) and Ce(IV)/Ce(III) in acidic media are commonly listed as +0.771 V and +1.76 V, respectively (*32*, *33*). For the ferroin/ferriin redox couple in 1 M H_2SO_4, the standard reduction potential of +1.04 V was measured (*34*). For the Ce^{4+}/Ce^{3+} couple of ammonium hexanitratocerate(IV) in 1 M H_2SO_4, the standard reduction potential of +1.44 V was reported (*35*). Hence, one must consider the oxidation of Fe^{2+} by Ce^{4+} (eq 5) (*36*, *37*).

Experimental and Mathematical Methods

Experimental Section

We followed the protocol reported by Shakhashiri (*31*) for the Ce/Fe-catalyzed bromate oxidation of MA. Three solutions were prepared. The first beaker contained 250 mL of deionized (DI) water and 9.5 g (57 mmol) of potassium bromate ($KBrO_3$, 99.5%). The second beaker contained 250 mL of DI water, 1.75 g (15 mmol) of potassium bromide (KBr, 99+%), and 8.0 g (77 mmol) of MA [$H_2C(COOH)_2$, 99%]. The third beaker contained 75 mL of 18.38 M sulfuric acid, 175 mL of DI water, and 2.65 g of cerium(IV) ammonium nitrate [$Ce(NH_4)_2(NO_3)_6$, >98%]. All three beakers contained 250 mL of solution. A fresh ferroin solution was prepared by mixing 100 mL DI water, 0.23 g (1.51 mmol) of iron(II) sulfate heptahydrate [$FeSO_4{\cdot}(H_2O)_7$, 99.999%], and 0.46 g (1.96 mmol) of 1,10-phenanthroline (99+%).

In a 1 L beaker on a stir plate, the first two solutions were mixed and the third solution was added, followed by 15 mL of the ferroin solution. The initial concentrations of this parent system, the OCR(1,1) reaction, were $[KBrO_3] = 74.36$ mM, $[KBr] = 19.22$ mM, $[MA] = 100.5$ mM, $[H_2SO_4] = 0.882$ M, $[Ce] = 6.319$ mM, $[Fe] = 0.1622$ mM, $[Ce]/[Fe] = 38.96$, and $[cat._{total}] = 6.481$ mM.

The reaction was recorded for 40 min with a Panasonic HC-V110 video camera mounted on a tripod and set approximately 1.5 m away from the reaction beaker. A white poster board was placed behind the reaction beaker, and the zoom on the camera was set to five times. HD Writer 2.0 software was used to edit the iFrame-formatted video and produce an mp4 file.

Mathematical Section: Video Analysis and Numerical Aspects

Image Selection and Conversion to Red–Green–Blue Matrices

The video-editing software Aoao Video to Picture Converter was used to convert the captured video to a series of JPEG images (*38*, *39*). The program Mathematica (*40*, *41*) was employed for image analysis. The images were imported and cropped to isolate the desired data. The cropped region needed to be in a location where the sample was not obstructed or changed. For example, the portion of the image in Figure 1 was selected to avoid the stirring rod in the beaker, the water distortion at the top, and the beaker label on the left side. In some cases, the middle of the beaker was also avoided if a water vortex formed because of high stirring speeds. The cropped images were converted to matrices of red–green–blue (RGB) values using the ImageData command (*41*).

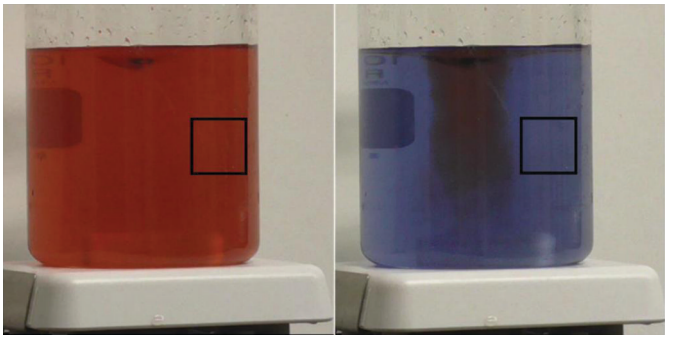

Figure 1. Sample window selection.

Distance from Characteristic Color Approach

The next step of the analysis involved the choice of a metric to compare the color of the cropped image to a predefined color target. Each image contained RGB data corresponding to the intensities of red, green, and blue on a scale from 0 to 255. The sum of the RGB values was used as in Beer's law to calculate species concentrations (*42*–*47*). A Fourier transform was applied to the data (*48*), and the digital-image-based method was employed to determine the end point of titrations (*49*, *50*). The square of a difference from a standard or reference color has also been used as a way of extracting concentrations from RGB data (*51*), and we took a similar approach.

For a given image with frame number *FN* corresponding to reaction time $t = FN/FPS$ (where FPS is frames per second), we chose the average relative distance from the characteristic color target values using the formula

$$DCC(t, R_c, G_c, B_c) = \frac{(1 - \sum_1^m \sum_1^n (id(i,j,1) - R_c)^2 + (id(i,j,2) - G_c)^2 + (id(i,j,3) - B_c)^2)}{m * n} \quad (6)$$

The $m \times n \times 3$ matrix *id* contains the R, G, and B values at the $m \times n$ points of the cropped image. The constant target values R_C, G_C, and B_C are the R, G, and B values predetermined for the characteristic target color. Equation 6 evaluates the deviation from the characteristic color, where $DCC = 1$ indicates no deviation. The characteristic colors "red," "blue1," and "yellow" are the RGB values of pure solution of the ions (Table 1). The characteristic colors "green" and "purple" were chosen based on those frames of OCR(1,1) that showed the cleanest and most intense green or purple coloring, respectively. The characteristic values for "blue2" are essentially half of the respective values for "blue1."

For a given characteristic color (R_C, G_C, B_C), the time traces values $DCC(t, R_C, G_C, B_C)$ were recorded over time. This approach recovers important timing information pertaining to the oscillating reactions because the time traces $DCC(t, R_C, G_C, B_C)$ are related to species concentration. The overall approach parallels the process of reflection UV-vis spectroscopy. The camera is the detector, and the computation of $DCC(t, R_C, G_C, B_C)$ for each image functions as a monochromator for the color (R_C, G_C, B_C). It is the main advantage of our approach to allow for the study of fast reactions at any target color (R_C, G_C, B_C) every 0.01 s. Time-resolved studies by UV-vis spectroscopy are limited by the time required to scan the entire visible range (ca. 3 s).

The Mathematica notebook for the determination of $DCC(t, R_C, G_C, B_C)$ values through the analysis of sets of images extracted from a video is shown in Figure 2. The code allows for the simultaneous analysis of as many color channels as desired. Interested parties may contact the corresponding author to obtain the notebook along with sample input and output files.

```
DCC Analyzer v1.2, 11-29-2018, Email: glaserr@mst.edu
Primary Author: Marco Downing
Team Members: Carmen Chicone, Rainer Glaser, Joseph Schell

SetDirectory["E:\Marco_DeLaRosa\BZR\BZR Image Folder\Shak_Fe_BZR_KpH0.18"]

b = Table[i, {i, 800805, 803847}];
(* image will have number in name.  Must include all numbers for all images
 in the folder *)
a = Table["Shak_Fe_BZR_KpH0.1" <> ToString[b[[i]]] <> ".jpg", {i, 1, Length[b]}];
(* folder name refers to series of images from video *)
c = Length[a]
Ips = 10.; (* 10 images per second.  Can change this parameter as desired. *)

p = Import[a[[12]]]; (* import sample image *)
o = ImageTake[p, {400, 450}, {575, 625}]
 (* choose desired region by changing numbers in brackets *)

channels = 6; (*defines the total number of channels to be analyzed*)
redchannel = List[0.764706, 0.035294, 0.039216];
(*characteristic RGB values listed in the order (R,G,B)*)
blue1channel = List[0.072606, 0.187665, 0.390992];
greenchannel = List[0.261962, 0.858040, 0.140393];
blue2channel = List[0.139660, 0.338500, 0.657990];
purplechannel = List[0.639216, 0.282353, 1.0];
yellowchannel = List[0.962219, 0.928007, 0.105122];
std = List[redchannel, blue1channel, greenchannel, blue2channel, purplechannel,
  yellowchannel] (*creates an array of the characteritic colors*)
std[[2, 1]] (*test to make sure array is working*)

list = Array[f, {c, channels + 1}];
Do[{in = Import[a[[i]]], im = ImageTake[in, {400, 450}, {575, 625}],
   id = ImageData[im], u = Dimensions[id], list[[i, 1]] = i / Ips,
   (* ImageTake numbers should match those for the sample above *)
   list[[i, z]] =
    (1 -
      ((Sum[((id[[k, j, 1]] - std[[z - 1, 1]])^2) +
           ((id[[k, j, 2]] - std[[z - 1, 2]])^2) + ((id[[k, j, 3]] - std[[z - 1, 3]])^2),
          {k, u[[1]]}, {j, u[[2]]}]) / (u[[1]] * u[[2]]))),
   If[Divisible[i, 1000], Print[i]]}, {i, 1, Length[a]}, {z, 2, channels + 1}];
Length[list] (* check of data extraction process *)

SetDirectory["C:\\Users\\jrsg24\\Desktop"]
Export["Shak_BZR_KpH0.18test.xls", list]
NotebookSave[]
```

Figure 2. Mathematica notebook to determine $DCC(t, R_C, G_C, B_C)$.

Effects of Frame Number

The choice of the number of FPS to use in the data analysis requires a balance between accuracy and computer time. In an mp4 format, the upper limit is given by the technical limit of 29 FPS. The selection of 29 FPS for the analysis provides the clearest data but at a very high processing time. Conversely, the selection of only 1 FPS limits the accuracy of the data analysis but allows quick

scanning of huge data sets. To determine which FPS rate is the best, finding the optimal balance between both processing time and accuracy really is the key issue.

Using a normalized root-mean-square (NRMS) deviation, we analyzed the percentage difference data at one FPS varied from the "ideal" 29 FPS data (Table 2). We chose 10 FPS as the most appropriate compromise between time and accuracy. The 10 FPS runs required only 70 min to analyze, versus 260 min for the 29 FPS runs, while only having an approximate 1% NRMS error. Conveniently, the maximum NRMS error was only approximately 4% at the 1 FPS runs, and so for quick analysis the method is still quite accurate.

Table 2. Numerical Aspects of Video Image Analysis: Processing Time for DCC(*t*, blue1) in Reaction OCR(1,1) with Frame Number and Window Size Dependence

Entry	*FPS*[a]	*Window Size*[b]	*NRMSD*[c] *(%)*	*ProcessingTime*[d] *(min)*
		FPS Dependence		
1	29	200 × 200	0.000	260.9
2	25	200 × 200	0.374	223.9
3	20	200 × 200	0.674	142.4
4	15	200 × 200	0.712	108.4
5	10	200 × 200	1.283	71.30
6	5	200 × 200	2.070	34.63
		Window Size Dependence		
7	10	200 × 200	0.000	71.30
8	10	200 × 100	1.356	60.68
9	10	100 × 100	1.777	56.80
10	10	100 × 50	2.204	54.56
11	10	50 × 50	2.182	50.56
12	10	50 × 25	3.025	49.20
13	10	25 × 25	2.970	46.96
14	10	10 × 10	3.139	47.04
15	10	5 × 5	5.617	45.77
16	10	1 × 1	5.023	46.34

[a] FPS = Frames per second. [b] Window size in pixels. [c] NRMSD = Normalized root-mean-square deviation. [d] Time required for the data integration.

Effects of Window Selection (Size and Location)

With the FPS set, standardizing the window selection is possible. While location is dependent on the application, the key criterion for the selection of the location is the requirement to avoid color distortions. In our applications, this meant avoiding the center where distortion occurred due to the vortex. The choice of the size of the window is constrained by the size of the distortion-free space and by practical limitations to the analysis time. The amount of time saved by selecting a smaller window

size is proportional to the number of FPS used. Higher FPS values mean more time gained or lost for increasing or decreasing window size.

Using 10 FPS, we found that the processing time needed when going from a 200 × 200 pixel window to just one pixel only changed from 70 to 45 min, a 35% decrease. However, this also introduced a 5% NRMS error. The data indicate that even reducing the frame from 200 × 200 pixels to 200 × 100 pixels introduced a 1.4% NRMS error while reducing the time by approximately 15%. We found using a 100 × 100 pixel window kept the NRMS error under 2% while reducing analysis time by 21%. Using both these methods, we reduced the calculation time by 80% while only introducing an NRMS error of approximately 3%.

Results and Discussion

Measurements of the Time Traces *DCC*(*t*)

Discrete plots were generated of the time traces *DCC*(*t*) for the OCR(1,1) reaction. The *DCC*(*t*) values were plotted for approximately 2900 s (48.3 min) for five characteristic colors (using blue1 but not blue2). The discrete plot of the time traces for reaction OCR(1,1) is shown in Figure 3, together with a close-up in the range $500 \leq t \leq 700$ s. The time traces *DCC*(*t*) determined in every color channel show oscillations with various shapes. We needed to develop parameters to characterize the period variations as a function of reaction time, examine their color-selection dependence, and extract mechanistic insights from this information.

Oscillation Pattern Analysis and Color-Base Selection

We analyzed the shapes of the time traces *DCC*(*t,* color) and found that two characteristic types occurred (Scheme 1). We refer to these shapes as the dromedary (one-humped camel) and Bactrian types (two-humped camel).

We began with the analysis of time traces with dromedary-shaped periods and specifically determined the times when *DCC*(*t,* color) goes through minima and maxima (Scheme 1, top). The time between successive maxima is the period. We also characterized the ascent times (oxidation times) and the descent times (reduction times) to and from the maxima, respectively. While a strictly periodic process is characterized by one period time, chemical oscillations feature period times that vary with reaction time. The data show that the timing characteristics for each oscillation cycle vary with the reaction progress, and we therefore report the timing characteristics for every oscillation over the course of the reaction. In most cases, the variations of the timing characteristics were steady and well-described with simple polynomials (Table 3). Parameters characterizing the oscillation patterns close to the reaction times of 500 and 2000 s are summarized in Table 4.

Method of Finding Extrema in DCC(t) and the Start of the Oxidation Phase

The local minima and maxima for the time traces *DCC*(*t*) were determined using Mathematica and the following process. First, the time trace *DCC*(*t*) data were smoothed using a moving-average filter computed by averaging over *k* frames. The averaging reduced the random noise and produced the time trace $DCC_A(t)$. Next, $DCC_A(t)$ was analyzed with an extrema-point finder function, which searches for local minima and maxima and generates the discrete functions $EPmax(t_i)$ (extrema points max) and $EPmin(t_j)$ (extrema points min). The period times $PT(t_i)$ were determined as the difference $PT(t_i) = t_{i+1} - t_i$.

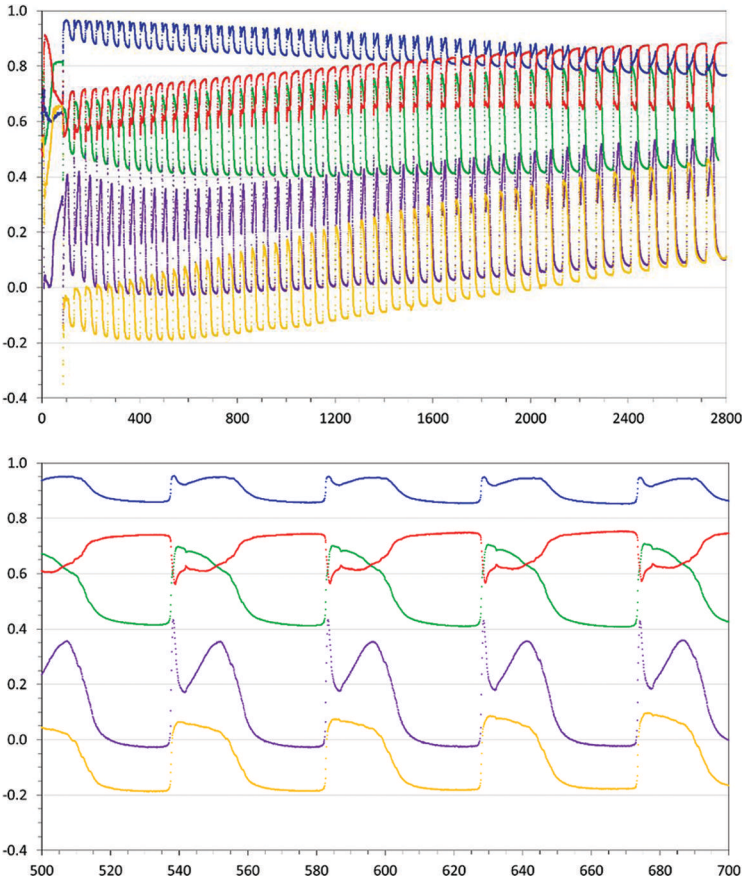

Figure 3. Discrete plots of DCC(t) values determined by image analysis of the video recording of OCR(1,1) for various characteristic colors.

The determination of the oxidation time $OT(t_i)$ leading up to peak $EPmax(t_i)$ and of the reduction time $RT(t_i)$ following that same peak are trivial for smooth time traces (Scheme 1, top). With the minima $EPmin(t_j)$ and $EPmin(t_{j+1})$ before and after the maximum $EPmax(t_i)$, respectively, the oxidation time is $OT(t_i) = t_i - t_j$, and the reduction time is $RT(t_i) = t_{j+1} - t_i$. However, the times traces are not always sufficiently smooth, and $EPmin(t_j)$ does not correspond to the actual onset of oxidation at time t_j^{ox}, with $t_j < t_j^{ox}$. Hence, we also determined t_j^{ox} and defined the oxidation time as $OT(t_i) = t_i - t_j^{ox}$ and the reduction time as $RT(t_i) = t_{j+1}{}^{ox} - t_i$.

With these definitions of $OT(t_i)$ and $RT(t_i)$, one can identify the maxima-based period time $PT(t_i) = t_{i+1} - t_i$ as the sum of $RT(t_i) = t_{j+1}{}^{ox} - t_i$ and $OT(t_{i+1}) = t_{i+1} - t_{j+1}{}^{ox}$. Alternatively, one can use the knowledge of the t_i^{ox} values and define the period as $PT^{ox}(t_j) = t_{j+1}{}^{ox} - t_j^{ox}$—that is, the time between successive onsets of metal oxidation. Note that as $PT^{ox}(t_j)$ equals the sum of $OT(t_i) = t_i - t_j^{ox}$ and $RT(t_i) = t_{j+1}{}^{ox} - t_i$, we will use this definition in the following discussion.

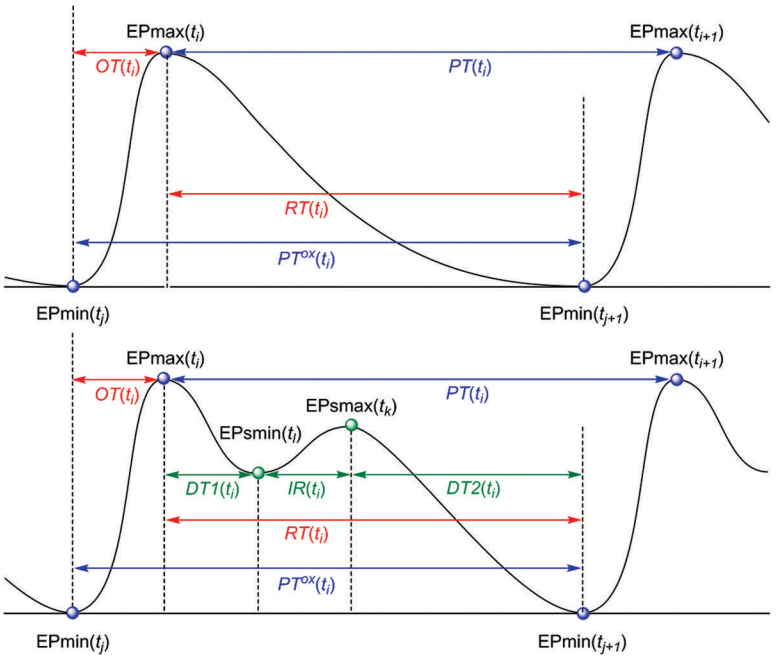

Scheme 1. Parameters in the oscillation pattern analysis of time traces with one maximum per period (dromedary-type, top) or two maxima per period (Bactrian-type, bottom).

The determination of t_j^{ox} employs an interpolation function $DCC_I(t)$ of the $DCC_A(t)$ data and involves a backward search starting at the maximum $EPmax(t_i)$. This method works well for time traces that feature steady increases along the entire ascent $\{d[DCC_I(t)]/dt \geq 0\}$, which usually occurs for time traces with oscillation periods of >20 s. To determine the ascent time to the *i*th maximum $EPmax(t_i)$, we examined $d[DCC_I(t)]/dt$ going backward from t_i and found the first point with $d[DCC_I(t)]/dt < 0$. The time of this point is defined as t_j^{ox}.

Period Variation, Oxidation Times, and Reduction Times in the Yellow Channel

Figure 4 shows the period times $PT^{ox}(t_i)$, the oxidation times $OT(t_i)$, and the reduction times $RT(t_i)$ as a function of time for the OCR(1,1) reaction. These data are the result of analysis of the time traces *DCC*(*t*, yellow). Table 3 shows the polynomial coefficients and the associated regression coefficients that best fit the measured data. In almost all cases, the measurements show a steady variation of the timing characteristic, and all data are included in the regression.

Table 3. Polynomial Coefficients and Regression Coefficients for Time Variations of Oscillation Parameters for Reaction OCR(1,1)[a]

Parameter[b]	*Channel*	*a*	*b*	*c*	*d*	R^2
			Primary Parameters			
$PT^{ox}(t_i)$	Yellow	−8E−10	9E−06	4.5E−03	44.997	0.9997
$RT(t_i)$	Yellow	−9E−10	8E−06	4E−03	38.817	0.9998
$OT(t_i)$	Yellow	−4E−11	9E−07	1.4E−03	6.592	0.9663
			Oxidation Times[c]			
$OT(t_i)$	Green[d]			0.9991	0.0	0.9496
			Primary Parameters			
$PT^{ox}(t_i)$	Blue	−1E−09	1E−05	−0.0064	45.990	0.9996
$RT(t_i)$	Blue	−1E−09	9E−06	−0.0051	43.378	0.9995
$OT(t_i)$	Blue	−2E−10	9E−07	−0.0014	2.623	0.8383
			Secondary Parameters			
$DT1(t_i)$	Blue	−2E−10	1E−06	−0.0019	3.731	0.9837
$IR(t_i)$	Blue	−1E−10	3E−06	−0.0039	12.175	0.9864
$DT2(t_i)$	Blue	−7E−10	5E−06	0.0007	27.499	0.9943
			Primary Parameters			
$PT^{ox}(t_i)$	Purple	−1E−09	1E−05	−0.0063	45.960	0.9995
$RT(t_i)$	Purple	−9E−10	9E−06	−0.0043	40.433	0.9998
$OT(t_i)$	Purple	−2E−10	1E−06	−0.0020	5.527	0.7608
			Secondary Parameters			
$DT1(t_i)$	Purple	−2E−10	1E−06	−0.0020	3.853	0.9834
$IR(t_i)$	Purple	−2E−09	1E−05	−0.0164	14.747	0.9897
$DT2(t_i)$	Purple	1E−09	−4E−06	0.0141	21.833	0.9991

[a] Trend line function: $y(t) = a \cdot t^3 + b \cdot t^2 + c \cdot t + d$. [b] PT = period time, RT = reduction time, DT1 = first drop time, IR = intermediate rise time, and DT2 = second drop time. [c] Trend line function: $DCC(t, \text{green}) = c \cdot DCC(t, \text{yellow}) + d$. [d] Trend line-based range: $0 < t < 1755$ s.

Table 4. Variations of Period Lengths and Pattern Shape Parameters with Reaction Time[a]

Reaction	*Channel*	*PT*	*RT*	*DT1*	*IR*	*DT2*	*IR+DT2*
		t = 500 s					
OCR(1,1)	Yellow	45	39				
OCR(1,1)	Blue	45	42	3	12	28	40
		t = 2000 s					
OCR(1,1)	Yellow	67	57				
OCR(1,1)	Blue	65	63	4	17	42	59

[a] Period time (PT), reduction time (RT), first drop time (DT1), intermediate rise time (IR), and second drop time (DT2) in seconds.

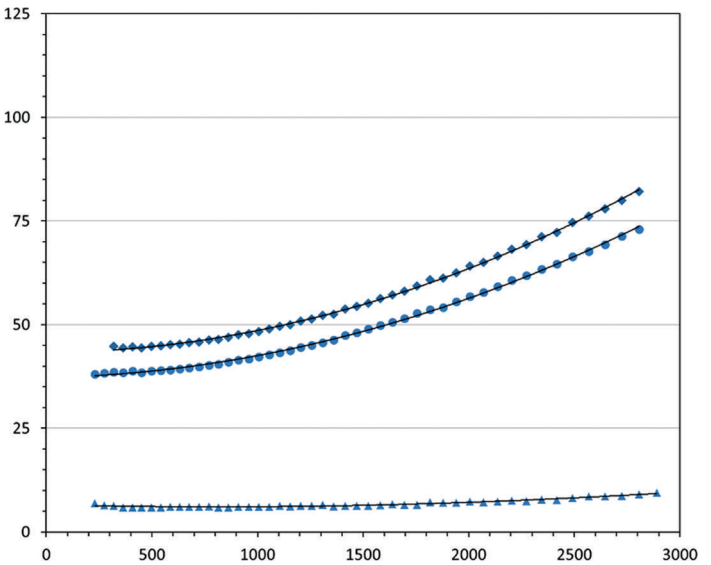

Figure 4. Oscillation pattern analysis for the OCR(1,1) reaction in the yellow channel. Variations over time are shown for period times $PT^{ox}(t_i)$ (diamonds), oxidation times $OT(t_i)$ (triangles), and reduction times $RT(t_i)$ (circles).

Figure 4 clearly illustrates that the period times $PT^{ox}(t_i)$ increase during the course of the reactions. $PT(t_i)$ and $RT(t_i)$ values for the cycles close to the reaction times of 500 and 2000 s are listed in Table 4. The reduction times $RT(t_i)$ are always much longer than the oxidation times. The variations of oxidation times over the course of the reaction are much more moderate than those of the reduction times.

Period Variation, Oxidation Times, and Reduction Times in the Green Channel

We analyzed the *DCC*(*t,* green) time traces the same way the *DCC*(*t,* yellow) traces were analyzed. Plots of *DCC*(*t,* green) versus *DCC*(*t,* yellow) show perfect linear correlations with unity slopes for the period times $PT^{ox}(t_i)$ and the reduction times $RT(t_i)$ (Figure 5).

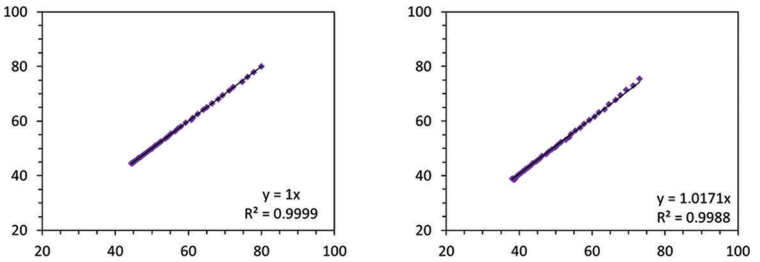

Figure 5. Oscillation pattern analysis for OCR(1,1): Comparison of the time traces DCC(t, yellow) (x-axis) and DCC(t, green) (y-axis). Variations over time are shown for period times $PT^{ox}(t_i)$ (left) and reduction times $RT(t_i)$ (right).

Period Variation, Oxidation Times, and Reduction Times in the Blue and Purple Channels

The analysis of the time traces in the blue and purple channels is made slightly more complicated by the fact that two maxima can appear within one period. Similar to the primary extrema $EPmax(t_i)$ and $EPmin(t_j)$, we defined $EPsmax(t_k)$ and $EPsmin(t_l)$ for the second feature (Scheme 1, bottom), and the additional parameters $DT1(t_i)$, $IR(t_i)$, and $DT2(t_i)$ were needed to describe the shapes. The first drop time $DT1(t_i)$ specifies the time between the first maximum $EPmax(t_i)$ and the second minimum $EPsmin(t_l)$ and is determined by $DT1(t_i) = t_l - t_i$. The intermediate rise time, which can be calculated as $IR(t_i) = t_k - t_l$, is the time between the second minimum $EPsmin(t_l)$ and the second maximum $EPsmax(t_k)$. The second drop time can be determined by $DT2(t_i) = t_{j+1} - t_k$ and is the time between the second maximum $EPsmax(t_k)$ and the following minimum $EPmin(t_{j+1})$. For the same reason discussed earlier, we used $t_{j+1}{}^{ox}$ instead of t_{j+1} so that $DT2(t_i) = t_{j+1}{}^{ox} - t_k$.

The results of the analysis of the $DCC(t_i$, blue) and $DCC(t_i$, purple) time traces of the OCR(1,1) reaction are illustrated in Figure 6. As with the analysis of the yellow channel, solid trend lines are shown for $PT^{ox}(t_i)$, $OT(t_i)$, and $RT(t_i)$, and dashed trend lines are shown for $DT1(t_i)$, $IR(t_i)$, and $DT2(t_i)$. The polynomial coefficients are listed in Table 3, and Table 4 lists representative values for t_i = 500 s and t_i = 2000 s. The first drop times $DT1(t_i)$ are always very short—less than 5 s.

Color-Base Dependency of the Oscillation Pattern Analysis

Plots of the respective trend lines created with the $DCC(t_i$, yellow), $DCC(t_i$, blue), and $DCC(t_i$, purple) data illustrate in a compelling fashion that the $PT^{ox}(t_i)$ time traces overlay perfectly for $t <$ 1500 s and in many cases for much longer (Figure 7). The oxidation times $OT(t_i)$ for $DCC(t_i$, blue) are always shorter than the oxidation times for $DCC(t_i$, yellow).

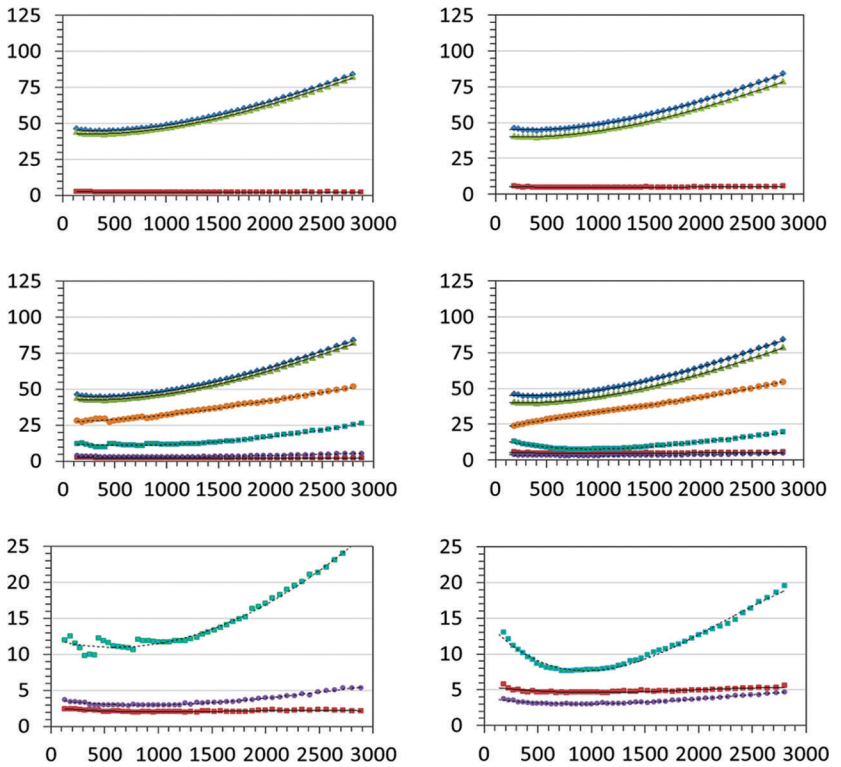

Figure 6. Oscillation pattern analysis for reaction OCR(1,1) in the blue channel (left) and purple channel (right). The top panels show the variation over time of the primary parameters: period times $PT^{ox}(t_i)$ (blue diamonds), oxidation times $OT(t_i)$ (red squares), and reduction times $RT(t_i)$ (green triangles). The panels in the middle show the primary parameters again but also include the variation over time of the secondary parameters: first drop times $DT1(t_i)$ (purple circles), intermediate rise times $IR(t_i)$ (teal squares), and second drop times $DT2(t_i)$ (orange circles). The bottom panels are zoomed-in versions of the center panels and show only the secondary parameters.

Kinetic Origin of the Bactrian-Type Oscillation Pattern of Fe(III)

In the Fe-only reactions, the time traces are of the dromedary type as expected; they show a short, single maximum in every cycle (*25*). In sharp contrast, however, every FC-BZR features a second maximum in the blue trace (Figure 3), and they are of the Bactrian-type. Scheme 2 is helpful in discussing the mechanism responsible for the variation of the Fe^{3+} concentration within one period of the FC-BZR, and we distinguish four phases.

Phase 1 involves the *oxidation* of the metal catalysts (eqs 1 and 2) by the active oxidant $BrO_2\cdot$ with oxidation rates $k_1[Fe^{2+}][BrO_2\cdot]$ and $k_2[Ce^{3+}][BrO_2\cdot]$, respectively. The reaction rate constants for the oxidations of Fe(II) and Ce(III) are $k_1 = 1.66\cdot10^7$ L/(mol·s) (*52*) and $k_2 = 6\cdot10^4$ L/(mol·s) (*53*, *54*), respectively. The reaction rates for iron oxidation will always exceed the reaction rates for cerium oxidation, even though $[Fe^{2+}]_0$ is a magnitude lower than $[Ce^{3+}]_0$. Phase 1 ends once all $BrO_2\cdot$ is exhausted by the oxidation of metals or organic compounds.

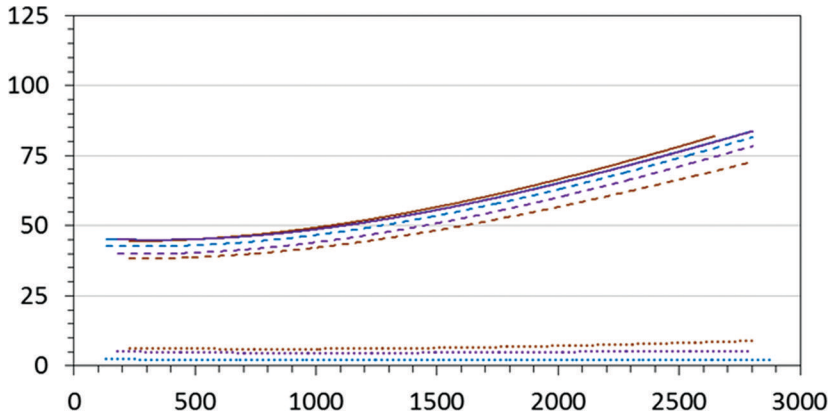

Figure 7. Color-base dependency of the oscillation pattern analysis of reaction OCR(1,1). Comparisons of the trend lines are fitted to the variations over time of the primary parameters from the time traces DCC(t, yellow) (brown), DCC(t, blue) (blue), and DCC(t, purple) (purple). Solid trend lines represent period times $PT^{ox}(t_i)$, dashed lines represent reduction times $RT(t_i)$, and dotted lines represent oxidation times $OT(t_i)$.

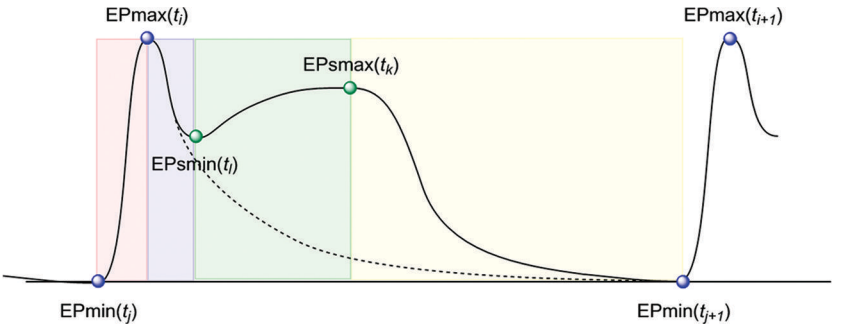

Scheme 2. Phases in the Fe^{3+} concentration within one period of the FC-BZR.

Phase 2 is the first stage of the *reduction* of Fe^{3+} and Ce^{4+} by BMA (eqs 3 and 4a) with reaction rates $k_3[Fe^{3+}][BMA]$ and $k_4[Ce^{4+}][BMA]$, respectively, and with $k_3 = 11.7$ L/(mol·s) and $k_4 = 0.09$ L/(mol·s), respectively (*55*–*57*). The reaction rate constant $k_4(MA) = 0.23$ L/(mol·s) (*56*, *58*) for the reduction of Ce^{4+} by MA is approximately 2.5 times higher than $k_4(BMA)$. The Fe^{3+} reduction (eq 3) is much faster than the Ce^{4+} reduction (eq 4). The high reaction rates for Fe^{3+} reduction ensure narrow peaks in the blue trace of Fe-only reactions, and this rapid Fe^{3+} decay is indicated by the dashed line in Scheme 2. In contrast, the much slower reduction of Ce^{4+} by BMA or MA proceeds during the entire duration of each period of the Ce-only reactions and never reaches completion.

Phase 3 begins once the rate of oxidation of Fe^{2+} by Ce^{4+} (eq 5) exceeds the rate of Fe^{3+} reduction by BMA. The rates for the formation of Fe^{3+} and Ce^{4+} are described by eqs 7 and 8, respectively. The occurrence of the Bactrian shape is the direct consequence of replacing the Ce^{4+} reduction by BMA (eq 4) with its reduction by Fe^{2+} (eq 5).

$$[Fe^{3+}]' = k_1[Fe^{2+}][BrO_2\cdot] - k_3[Fe^{3+}][BMA] + k_5[Ce^{4+}][Fe^{2+}] \quad (7)$$

$$[Ce^{4+}]' = k_2[Ce^{3+}][BrO_2\cdot] - k_4[Ce^{4+}][BMA] - k_5[Ce^{4+}][Fe^{2+}] \quad (8)$$

The reaction rate constant for the redox reaction of eq 5 is $k_5 = 1.61 \cdot 10^5$ L/(mol·s)[8] in 1 M H_2SO_4 and six orders of magnitude higher than k_4. The concentration of BMA must be less than the initial concentration of MA ($[MA]_0 = 100$ mM), and it can be at most two to three magnitudes larger than the maximal concentration of the iron catalyst ($[Fe]_0 = 0.16$ mM). The concentration terms will never make up for the difference between k_4 and k_5, and hence the reaction of Ce^{4+} with Fe^{2+} becomes the dominant mechanism of Ce^{4+} reduction. Bromide recycling becomes highly effective because Fe^{3+} reduction always produces bromide (while Ce^{4+} reduction may not).

Both Ce^{4+} and Fe^{2+} must be present in significant amounts for the reaction in eq 5 to become productive. Equation 5 is not important at the very beginning of the period for lack of Ce^{4+}. In the course of phase 1 (eqs 1 and 2), the concentration of Ce^{4+} builds up and eq 5 can operate, but it can only do so for a very brief time because eq 1 depletes the concentration of Fe^{2+} quickly ($k_1 \gg k_2$). The onset of phase 3 occurs when both Ce^{4+} and Fe^{2+} become available in significant concentrations and the $k_5[Ce^{4+}][Fe^{2+}]$ term drives the Fe^{3+} concentration up to its second maximum.

Phase 4 starts with the decline of the Ce^{4+} concentration, and the oxidation of Fe^{2+} by Ce^{4+} (eq 5) cannot keep up with Fe^{3+} reduction by BMA (eq 3).

Conclusions

We have developed a new video-based approach for the analysis of the kinetics of oscillating reactions that mathematically mimics reflection UV-vis spectroscopy. The main advantage of our approach is that it allows the study of fast reactions at any target color (R_C, G_C, B_C) at the same time and with a temporal resolution of 0.01 s. The image analysis results in discrete time traces $DCC(t, R_C, G_C, B_C)$, and we described numerical methods for the analysis of the quasiperiodic oscillation patterns over the course of the reactions.

We have demonstrated that this new approach yields accurate period lengths $PT(t)$ that are independent of the choice of the color base. This approach also recovers important timing information about the evolution of the redox chemistry of the catalysts within each period because the time traces $DCC(t, R_C, G_C, B_C)$ are related to species concentration.

The most important mechanistic result of the present study is the discovery of the Bactrian-type oscillation pattern of Fe(III) in the FC-BZR: Fe(III) goes through two maxima in every period. A chemical mechanism was proposed to explain this Bactrian-type oscillation pattern. The outstanding feature of the Ce/Fe-catalyzed FC-BZR in BMA-rich environments is the effective redox-cycling of the metal catalysts ($[M]_{rc} \approx [Ce]_0 + [Fe]_0$) and the effective bromide recycling (BMA oxidation » MA oxidation).

An analysis of the Bactrian-type oscillation pattern of the Fe catalyst as a function of the Ce/Fe concentration ratio is now underway to further probe the kinetics. Yet there are limitations to one's capacity to rationalize complex systems of reactions based on experimentation alone. Clearly, simulations of the entire reaction system will be needed to fully understand the details of the FC-BZR over time, and the measured data (Tables 3 and 4) provide a wealth of constraints to determine chemically reasonable parameters. In particular, simulations should aim to reproduce the temporal evolution of those characteristic parameters, which show the least experimental noise.

Acknowledgements

This research was supported by the National Science Foundation (PRISM 0928053; CHE 0051007), and we acknowledge the donors of the American Chemical Society Petroleum Research Fund for partial support of this research (PRF-53415-ND4).

References

1. Zhabotinsky, A. M.; Zaikin, A. N. Concentration Wave Propagations in Two-Dimensional Liquid-Phase Self-Oscillating System. *Nature* **1970**, *225*, 535–537.
2. *Oscillations and Traveling Waves in Chemical Systems*; Field, R. J., Burger, M., Eds.; Wiley: New York, 1985.
3. Belousov, B. P. A Periodic Reaction and its Mechanism. *Appendix in Oscillations and Traveling Waves in Chemical Systems*; Field, R. J., Burger, M., Eds.; Wiley: New York, 1985; pp 605–660.
4. Epstein, I. R.; Kustin, K.; De Kepper, P.; Orban, M. Oscillating Chemical Reactions. *Sci. Am.* **1983**, *248*, 112–146.
5. Field, R. J.; Koros, E.; Noyes, R. M. Oscillations in Chemical Systems. II. Thorough Analysis of Temporal Oscillation in the Bromate-Cerium-Malonic Acid System. *J. Am. Chem. Soc.* **1972**, *94*, 8649–8664.
6. Jinguji, M.; Ishihara, M.; Nakazawa, T. Photoinduced Formation of Spatial Patterns in the Belousov-Zhabotinskii Reaction. *J. Phys. Chem.* **1990**, *94*, 1226–1229.
7. Srivastava, P. K.; Mori, Y.; Hanazaki, I. Dual-Frequency Chemical Oscillators with Acetylphenols as Substrates. *J. Phys. Chem.* **1991**, *95*, 1636–1639.
8. Gyenge, R.; Körös, E.; Tóth, K.; Pungor, E. The Critical Bromide Concentration in an Oscillating Chemical System. *Anal. Chim. Acta* **1978**, *98*, 385–387.
9. Körös, E.; Burger, M.; Friedrich, V.; Adány, L. Chemistry of Belousov-Type Oscillating Reactions. *Faraday Symp. Chem. Soc.* **1974**, *9*, 28–37.
10. Sobel, S. G.; Hastings, H. M.; Field, R. J. Oxidation State of BZ Reaction Mixtures. *J. Phys. Chem. A* **2006**, *110*, 5–7.
11. *An Introduction to Nonlinear Chemical Dynamics: Oscillations, Waves, Patterns, and Chaos*; Epstein, I. R., Pojman, J. A., Eds.; Oxford University Press: New York, 1998.
12. Gray, P.; Scott, S. K. *Chemical Oscillations and Instabilities: Non-Linear Chemical Kinetics*; Oxford University Press: New York, 1994.
13. *Chaos in Chemistry and Biochemistry*; Field, R. J., Gyorgyi, L., Eds.; World Scientific Pub. Co.: Hackensack, NJ, 1993.
14. Strogatz, S. H. *Nonlinear Dynamics and Chaos: With Applications to Physics, Biology, Chemistry, and Engineering (Studies in Nonlinearity)*; Westview Press: Boulder, CO, 2001.
15. Fuchs, A. *Nonlinear Dynamics in Complex Systems: Theory and Applications for the Life-, Neuro- and Natural Sciences*; Springer: New York, 2013.
16. Verhulst, F. *Nonlinear Differential Equations and Dynamical Systems (Universitext)*; Springer: New York, 2013.
17. Glaser, R.; Jost, M. Disproportionation of Bromous Acid HOBrO by Direct O-Transfer and via Anhydrides $O(BrO)_2$ and BrO-BrO_2. An Ab Initio Study of the Mechanism of a Key Step of the Belousov-Zhabotinsky Oscillating Reaction. *J. Phys. Chem. A* **2012**, *116*, 8352–8365.

18. Glaser, R.; Camasta, C. Electronic Structures and Spin Density Distributions of BrO_2 and $(HO)_2BrO$ Radicals. Mechanisms for Avoidance of Hypervalency and for Spin Delocalization and Spin Polarization. *Inorg. Chem.* **2013**, *52*, 11806–11820.
19. Glaser, R.; Delarosa, M.; Salau, A. O. Why the Acidity of Bromic Acid Really Matters for Kinetic Models of Belousov-Zhabotinsky Oscillating Chemical Reactions. *J. Thermodyn. Catal.* **2013**, *4*, e115–e116.
20. Agreda, B. J. A.; Field, R. J. Activation Energy for the Disproportionation of $HBrO_2$ and Estimated Heats of Formation of $HBrO_2$ and BrO_2. *J. Phys. Chem.* **2006**, *110*, 7867–7873.
21. Glaser, R. E.; Delarosa, M. A.; Salau, A. O.; Chicone, C. Dynamical Approach to Multi-Equilibria Problems for Mixtures of Acids and Their Conjugated Bases. *J. Chem. Educ.* **2014**, *91*, 1009–1016.
22. Zars, E.; Schell, J.; Delarosa, M.; Chicone, C.; Glaser, R. Dynamical Approach to Multi-Equilibria Problems Considering Debye-Hückel Theory of Electrolyte Solutions. Concentration Quotients as a Function of Ionic Strength. *J. Solution Chem.* **2017**, *46*, 1–20.
23. Schell, J.; Zars, E.; Chicone, C.; Glaser, R. Simultaneous Determination of All Species Concentrations in Multi-Equilibria for Aqueous Solutions of Dihydrogen Phosphate Considering Debye-Hückel Theory. *J. Chem. Eng. Data* **2018**, *63*, 2151–2161.
24. Muelleman, A.; Glaser, R. Learning to Read Spectra: Teaching Decomposition with Excel in a Scientific Writing Course. *J. Chem. Educ.* **2018**, *95*, 476–481.
25. Zars, E.; Glaser, R.; Downing, M.; Chicone, C. Measurements and Simulations of the Acidity Dependence of the Kinetics of the Iron-Catalyzed Belousov-Zhabotinsky Reaction. Proton-Catalysis in the Electron Transfer Reaction Involving the $[Fe(phen)_3]^{3+}$ Species. *J. Phys. Chem. A* **2018**, *122*, 6183–6195.
26. Lefelhocz, J. F. The Color Blind Traffic Light: An Undergraduate Kinetics Experiment Using an Oscillating Reaction. *J. Chem. Educ.* **1972**, *49*, 312–314.
27. Bruice, T.; Kasperek, G. Observations on an Oscillating Reaction. The Reaction of Potassium Bromate, Ceric Sulfate, and a Dicarboxylic Acid. *Inorg. Chem.* **1971**, *10*, 382–386.
28. Ruoff, P.; Sjøgren, C. E.; Kolboe, S. Transitions between Two Oscillatory States in a Closed Malonic Acid Belousov-Zhabotinsky Reaction Simultaneously Catalyzed by Ferroin and Cerium Ions. *Chem. Phys. Lett.* **1986**, *130*, 72–75.
29. D'Alba, F.; Di Lorenzo, S. Influence of Mixed Cerium(IV) Sulphate and Ferroin Catalysts on the Oscillatory Redox Reaction Between Malonic Acid and Bromate. *J. Chem. Soc., Faraday Trans.* **1987**, *83*, 267–270.
30. D'Alba, F.; Di Lorenzo, S. Control of the Oscillation Parameters in the Belousov-Zhabotinsky System by Means of Mixed Catalysts. *Bioelectrochem. Bioener.* **1987**, *17*, 243–252.
31. Shakhashiri, B. Z. *Chemical Demonstrations*; The University of Wisconsin Press: Madison, WI, 1985; Vol. 2, p 257.
32. WebElements Periodic Table of the Elements. www.webelements.com (accessed Nov. 30, 2018).
33. Bard, A. J.; Parsons, R.; Jordan, J. *Standard Potentials in Aqueous Solution*; Monographs in Electroanalytical Chemistry and Electrochemistry; Marcel Dekker: New York, 1985.
34. Nemcova, I.; Cermakova, L.; Gasparic, J. *Spectrophotometric Reactions*; Practical Spectroscopy Series; Marcel Dekker: New York, 1996; Vol. 22, p 159.

35. Binnemans, K. Applications of Tetravalent Cerium Compounds. In *Handbook on the Physics and Chemistry of Rare Earths*, 1st ed.; Gschneidner, K. A., Bunzli, J.-C., Pecharsky, V., Eds.; Elsevier: Amsterdam, 2006; Vol. 36, pp 281–392.
36. Sutin, N. Electron Transfer Reactions in Solution: A Historical Perspective. In *Advances in Chemical Physics: Electron Transfer - From Isolated Molecules to Biomolecules. Part 1*; Jortner, J., Bixon, M., Eds.; Wiley: New York, 1999; Vol. 106, pp 7−33.
37. Dulz, G.; Sutin, N. The Kinetics of the Oxidation of Iron(II) and its Substituted tris-(1,10-Phenanthroline) Complexes by Cerium(IV). *Inorg. Chem.* **1963**, *2*, 917–921.
38. Aoao Photo. http://www.aoaophoto.com (accessed Oct. 17, 2018).
39. Aoao Video to Picture Converter. http://www.aoaophoto.com/video-to-picture-converter/video-to-picture.htm (accessed Oct. 17, 2018).
40. Wolfram Research, Inc. *Mathematica*, Version 10.2; Champaign, IL, 2015. http://www.wolfram.com/mathematica/ (accessed Oct. 17, 2018).
41. Wolfram Language & System Documentation Center: ImageData Function. https://reference.wolfram.com/language/ref/ImageData.html (accessed Oct. 17, 2018).
42. Maleki, N.; Safavi, A.; Sedaghatpour, F. Single-Step Calibration, Prediction and Real Samples Data Acquisition for Artificial Neural Network Using a CCD Camera. *Talanta* **2004**, *64*, 830–835.
43. Firdaus, M. L.; Alwi, W.; Trinoveldi, F.; Rahayu, I.; Rahmidar, L.; Warsito, K. Determination of Chromium and Iron Using Digital Image-based Colorimetry. *Procedia Environ. Sci.* **2014**, *20*, 298–304.
44. dos Santos Benedetti, L. P.; dos Santos, V. B.; Silva, T. A.; Filho, E. B.; Martins, V. L.; Fatibello-Filho, O. A Digital Image-Based Method Employing a Spot-Test for Quantification of Ethanol in Drinks. *Anal. Methods* **2015**, *7*, 4138–4144.
45. Kohl, S. K.; Landmark, J. D.; Stickle, D. F. Demonstration of Absorbance Using Digital Color Image Analysis and Colored Solutions. *J. Chem. Educ.* **2006**, *83*, 644–646.
46. Huang, W. E.; Smith, C. C.; Lerner, D. N.; Thornton, S. F.; Oram, A. Physical Modelling of Solute Transport in Porous Media: Evaluation of an Imaging Technique Using UV Excited Fluorescent Dye. *Water Res.* **2002**, *36*, 1843–1853.
47. Li, W.; Zhang, R.; Wang, H.; Jiang, W.; Wang, L.; Li, H.; Wu, T.; Du, Y. Digital Image Colorimetry Coupled with a Multichannel Membrane Filtration-Enrichment Technique to Detect Low Concentration Dyes. *Anal. Methods* **2016**, *8*, 2888–2894.
48. Lopez-Molinero, A.; Cubero, V. T.; Irigoyen, R. D.; Piazuelo, D. S. Feasibility of Digital Image Colorimetry - Application for Water Calcium Hardness Determination. *Talanta* **2013**, *103*, 236–244.
49. da Nobrega Gaiao, E.; Martins, V. L.; da Silva Lyra, W.; de Almeida, L. F.; da Silva, E. C.; Araújo, M. C. U. Digital Image-Based Titrations. *Anal. Chim. Acta* **2006**, *570*, 283–290.
50. Tôrres, A. R.; da Silva Lyra, W.; de Andrade, S. I. E.; Andrade, R. A. N.; da Silva, E. C.; Araújo, M. C. U.; da Nóbrega Gaião, E. A Digital Image-Based Method for Determining of Total Acidity in Red Wines Using Acid–Base Titration Without Indicator. *Talanta* **2011**, *84*, 601–606.
51. Dong, W.; Selvadurai, A. P. S. Image Processing Technique for Determining the Concentration of a Chemical in a Fluid-Saturated Porous Medium. *Geotech. Test. J.* **2006**, *29*, 1–7.

52. Zhabotinsky, A.; Bucholtz, F.; Kiyatkin, A.; Epstein, I. Oscillations and Waves in Metal-Ion-Catalyzed Bromate Oscillating Reactions in Highly Oxidized States. *J. Phys. Chem.* **1993**, *97*, 7578–7584.
53. Hegedüs, L.; Wittmann, M.; Noszticzius, Z.; Yan, S.; Sirimungkala, A.; Försterling, H.-D.; Field, R. J. HPLC Analysis of Complete BZ Systems. Evolution of the Chemical Composition in Cerium and Ferroin Catalysed Batch Oscillators: Experiments and Model Calculations. *Faraday Discuss.* **2001**, *120*, 21–38.
54. Field, R. J.; Försterling, H.-D. On the Oxybromine Chemistry Rate Constants with Cerium Ions in the Field-Koros-Noyes Mechanism of the Belousov-Zhabotinskii Reaction: The Equilibrium $HBrO_2 + BrO_3^- + H^+ \rightleftarrows 2\,BrO_2\cdot + H_2O$. *J. Phys. Chem.* **1986**, *90*, 5400–5407.
55. Hegedüs, L.; Försterling, H.-D.; Onel, L.; Wittmann, M.; Noszticzius, Z. Contribution to the Chemistry of the Belousov-Zhabotinsky Reaction. Products of the Ferriin-Bromomalonic Acid and Ferriin-Malonic Acid reactions. *J. Phys. Chem. A* **2006**, *110*, 12839–12844.
56. Försterling, H.-D.; Stuk, L.; Barr, A.; McCormick, W. Stoichiometry of Bromide Production from Ceric Oxidation of Bromomalonic Acid in the Belousov-Zhabotinskii Reaction. *J. Phys. Chem.* **1993**, *97*, 2623–2627.
57. Chou, Y. C.; Lin, H. P.; Sun, S. S.; Jwo, J. J. Kinetic Study of the Ferriin Oxidation of Malonic Acid and its Derivatives. Implication in the Belousov-Zhabotinsky Reaction. *J. Phys. Chem.* **1993**, *97*, 8450–8457.
58. Sengupta, K. K.; Aditya, S. Kinetics and Mechanism of the Oxidation of Malonic Acid by Ceric Salts. *Z. Phys. Chem. (Muenchen, Ger.)* **1963**, *38*, 25–35.